NUMERICAL ANALYSIS OF THE "FERRIS WHEEL" MICE EXPOSURE SYSTEM USING AN EFFICIENT CYLINDRICAL FDTD SCHEME

P. Russo[†], A. Faraone[††]

[†] University of Ancona, Dipartimento di Elettronica ed Automatica
Via Brecce Bianche, 60131 Ancona, Italy

[††] Motorola Labs, Corporate EME Research Lab
8000 W. Sunrise Blvd., Fort Lauderdale, FL 33322, USA

The objective of this study is to develop a numerical tool for characterizing the "ferris wheel" exposure system employed in a long-term study of RF exposure on mice [5]. The "ferris wheel" is a radial cavity loaded with forty mice around its perimeter. In order to exploit the angular periodicity of the radial exposure system, we developed a Finite Difference in Time Domain (FDTD) code based on a cylindrical grid to analyze a single angular sector of the 40-mouse "ferris wheel". The singularity of the Maxwell equations in the cylindrical FDTD scheme was appropriately removed, and other suitable expedients were implemented to reduce simulation time and memory requirements. In order to estimate RF leakage, the actual openings in the radial cavity, needed to insert the mice, were considered as well. The FDTD scheme incorporates the perfectly matched layer (PML) *unsplit* formulation (anisotropic medium), as absorbing boundary condition. The code was validated with measurements, showing good agreement. A criterion for assessing the uniformity of the exposure is presented, together with results at 900 MHz and 1.8 GHz.

1. INTRODUCTION

Potential biological effects of non-ionizing electromagnetic radiation can be investigated by carrying out long-term animal exposure studies [1]-[3]. The animals should be placed inside exposure systems that ensure delivery of known *specific absorption rate* (SAR) [4] levels, which are precisely quantifiable throughout the study. Therefore an important issue arises concerning the design of the animal exposure system. Inside the system, the animals are exposed to RF energy with given signal characteristics (frequency and modulation). Control of the main exposure parameters that eventually dictate the dose of RF energy to the animals (e.g., incident field strength and polarization) is one key point of the study. Since there is a need to correlate SAR levels to any observed biological effect, knowledge of the SAR distribution inside the animal is very important.

In this paper, we present the development of a numerical tool for RF dosimetry inside an exposure system presently employed in a long-term study on transgenic mice exposed to GSM (Global System for Mobile communication) modulated fields at 900 MHz [5]. The exposure system was conceived and designed at the Motorola Labs in

Fort Lauderdale, Florida, and fifteen units were deployed at the Institute of Medical and Veterinary Science in Adelaide, South Australia, in the spring of 1999. Its main features are: (a) plane-wave like incident fields, with equal exposure conditions among the animals and good uniformity of the field inside each of them; (b) precisely quantifiable whole-body average SAR, with nominal values of 4, 2, 1, 0.25, and 0 W/kg (*sham exposed*) for different mice populations.

The "ferris wheel" exposure system comprises a radial waveguide that is fed so to excite the cylindrical TEM mode, short-circuited at the perimeter to form a radial cavity. Forty mice are positioned with the longer body axis parallel to the incident electric field, in a periodical angular pattern, so ideally the RF power is equally distributed among the mice. Fairly uniform collective long-term exposure among mice is the key for a well designed study.

Since the system has a cylindrical structure, we developed an FDTD code in cylindrical coordinates. The simulated results show favorable comparison with measurements. The uniformity of the SAR level inside the animals has been analyzed for the 900 MHz exposure system, as well as for the 1.8 GHz case. The latter exposure configuration is likely to be used in the near future upon minor modifications to the present "ferris wheel" design.

2. DESCRIPTION OF THE "FERRIS WHEEL" EXSPOSURE SYSTEM

The 900 MHz "ferris wheel" exposure system was described in [5] and is illustrated in Fig.1. Due to design constraints, such as exposure uniformity, available RF power and number of exposed animals, the resulting outcome was a radial cavity with 48-cm radius and 10-cm height. The system has been designed so that the mice are illuminated by a free-space like TEM wave. For the sake of completeness, we summarize briefly the main system characteristics. Inside the empty cavity, the TEM field components can be expressed in the cylindrical reference frame of Fig. 2 as

$$E_z(\rho) = A_r H_0^{(1)}(k\rho) + A_f H_0^{(2)}(k\rho),\qquad(1)$$

$$H_\phi(\rho) = \frac{j}{\eta}\left[A_r H_1^{(1)}(k\rho) + A_f H_1^{(2)}(k\rho)\right],\qquad(2)$$
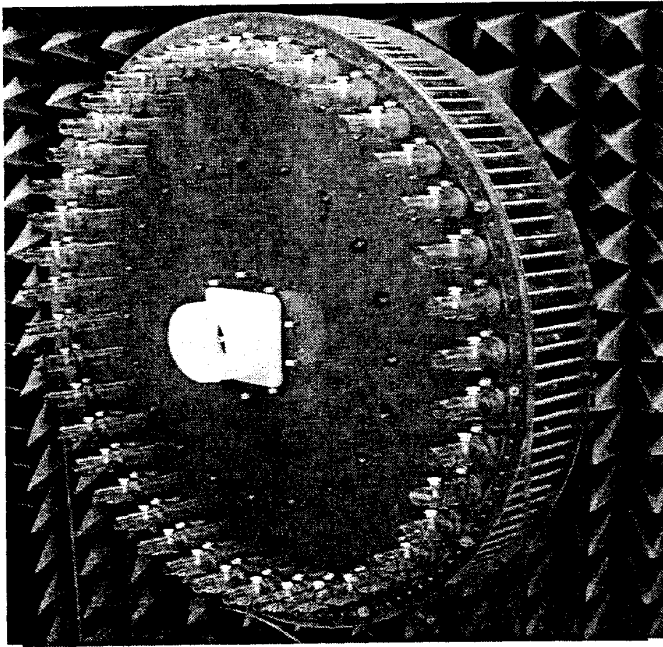
Fig. 1 Picture of the "ferris wheel" mice exposure system. The radial cavity is loaded with forty mice placed inside plastic holders that are periodically distributed around the perimeter. Holders are not considered in the simulations.

where k is the complex wavenumber, η is the wave impedance, and $H_v^{(1)}$, $H_v^{(2)}$ are v^{th} order Hankel functions describing the inward and outward cylindrical TEM waves.

Looking at (1) and (2), we notice that when the mice are placed inside the cavity, they can be considered exposed to an incident TEM-like wave. Moreover, if their position is removed from the excitation region (cavity center) and the frequency is such that longitudinal (z-varying) higher order modes are below cut-off, the perturbation of the incident field occurs mainly in the region around the animal. In this case, the mice are placed with their body axis at 44 cm from the "ferris wheel" center, co-polarized with the incident electric field. Such a position enhances the
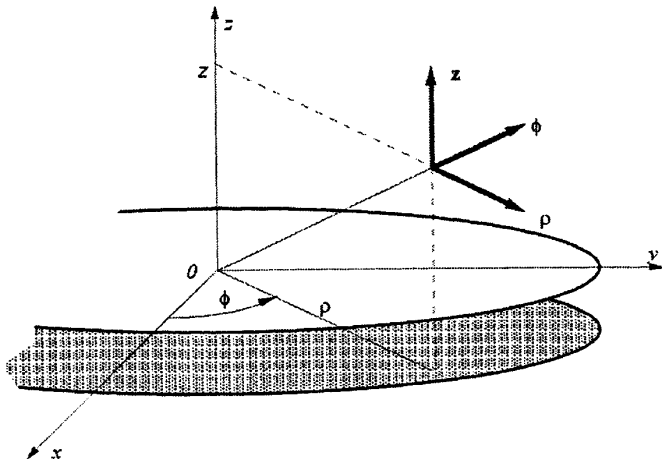

Fig.2 Reference frame associated with the radial cavity.

efficiency of the cavity [5].

The exposure system is fed through a tunable co-axial-to-cavity transition designed to ensure good impedance match for different loading conditions, i.e., mice position, size, and posture. As depicted in Fig. 3, a top-loaded monopole antenna that is capacitively coupled with a passive counterpoise, thus forming a series-stub tuning element forms the transition. Good impedance match of the loaded cavity is achieved adjusting the capacitive coupling between counterpoise and monopole. The mice change the incident field characteristics and alter its uniformity. Equations (1) and (2) cannot be employed to assess SAR uniformity inside the animal. On the other hand, SAR measurements everywhere inside the animal is extremely difficult, if not impossible. For this reason an FDTD code was developed to perform the analysis, which is the object of the present work. We used the simplified dummy models
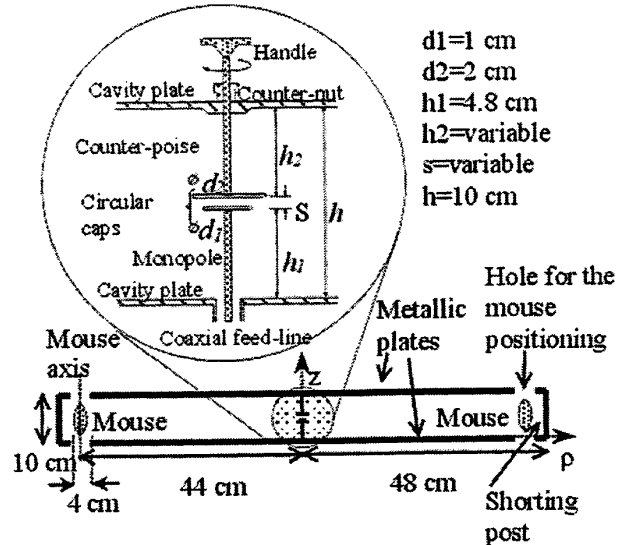

Fig.3 Sketch of the transition from the coaxial feed-line to the tunable cavity exciter. Holes at the structure's perimeter allow mice insertion and positioning.

instead of realistic mice models to validate the code. This approach allowed direct correlation with measurements already performed during the experimental characterization of the system [5], when dummies (30 cc plastic bottles filled with tissue simulant) were used because of the inconvenience of using live or dead mice during the long development phase. The numerical analysis of the SAR distribution in realistic FDTD mouse phantoms inside the "ferris wheel" will be the subject of a separate publication.

3.   NUMERICAL APPROACH

The complexity of the cavity's geometry and the mice tissue heterogeneity encouraged us to develop an in-house FDTD code for the analysis. Because the "ferris wheel" geometry (Fig.1) conforms to a cylindrical reference frame, the code was developed in cylindrical coordinates. The
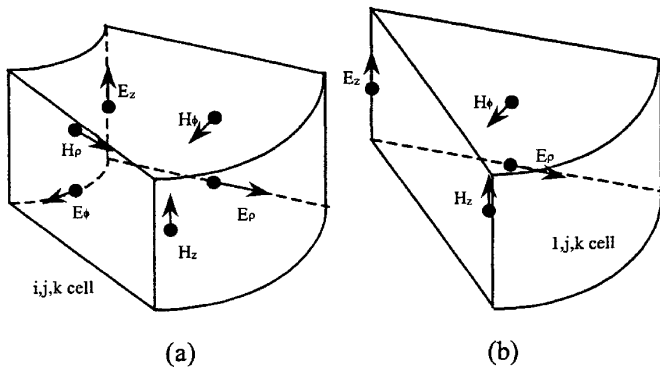
(a)   (b)

*Fig.4 (a) FDTD cylindrical unit-cell with associated field components. The cell is numbered with the i,j,k indices.
(b) Degenerated wedge cell at the ρ=0 axis, together with the relevant components. The cell number is (1,j,k).*

FDTD scheme employs the Yee unit-cell [6] to discretize the computational domain. The main challenges encountered were the singularity of the discretized Maxwell equations, as well as the code's run-time and memory requirements.

Treatment of the singularity

Yee unit-cell in cylindrical coordinates is depicted in Fig. 4a. The Maxwell equations feature a singularity on the line $\rho=0$, where the cell degenerates into a wedge as shown in Fig. 4b. The E_ϕ and H_ρ components, which are used to update E_z and H_z, are undefined on this axis. Therefore, we can use the conventional FDTD algorithm to update all components except for the latter, which require a different approach. For updating E_z, we discretized Ampere's law

$$\varepsilon\frac{\partial E_z}{\partial t} = \oiint H_\phi \rho \, d\phi \approx \sum_i H_\phi \, \rho \Delta\phi \quad . \qquad (3)$$

Therefore, we only need H_ϕ for updating the E_z component. For the H_z component we can use a more complicated approach [7], whose implementation is indeed quite simple in this case. Consider the equation for updating H_z

$$-\mu\frac{\partial H_z}{\partial t} = \frac{1}{\rho}\frac{\partial(\rho E_\phi)}{\partial\rho} - \frac{1}{\rho}\frac{\partial E_\rho}{\partial\phi}, \qquad (4)$$

which, upon discretization, becomes

$$-\mu\frac{H_z^n(i+\tfrac{1}{2},j+\tfrac{1}{2},k) - H_z^{n-1}(i+\tfrac{1}{2},j+\tfrac{1}{2},k)}{\Delta t} = \frac{1}{\rho(i)+\Delta\rho} \cdot$$

$$\frac{\rho(i+1)E_\phi^{n-1/2}(i+1,j+\tfrac{1}{2},k) - \rho(i)E_\phi^{n-1/2}(i,j+\tfrac{1}{2},k)}{\Delta\rho} -$$

$$\frac{1}{\rho(i)+\Delta\rho}\frac{E_\rho^{n-1/2}(i+\tfrac{1}{2},j+1,k) - E_\rho^{n-1/2}(i+\tfrac{1}{2},j,k)}{\Delta\phi}, \quad (5)$$

where i, j, k are the cell numbers in the three directions ρ, ϕ, and z, respectively, n is the time step, and the ½ increment in the subscript denotes field component interleaving. The wedge cell is characterized by $\rho(i)=0$, so the discretized equation is not singular at the $\rho=0$ line.

In a first approximation, the "ferris wheel" exhibits a cylindrical symmetry since the loads (mice) are electrically close to each other and far from the source. Therefore, as long as we stay near the $\rho=0$ axis, the cylindrical symmetry of the field distribution is minimally perturbed. Consequently the E_ϕ component is negligible in this zone, and so is its ρ-derivative. Under this assumption, we neglected the first term on the right-hand side of (4), so the equation becomes very simple for the closest FDTD cell, needing only E_ρ for updating the H_z component. This problem has also been addressed by Chen *et al.* [8] and solved using a similar approach, although they used a 2-D cylindrical coordinate system. In their approach Eq. (5) would be applied as is, provided that $\rho(i)$ vanishes in the first cell.

Memory requirements

An important aspect of a cylindrical FDTD implementation is the memory requirement, due to the increasing voxels dimension with the ρ coordinate. If we need a fine discretization far from the $\rho=0$ axis, voxels near the axis will be very thin. This generates over-sampling of the volume around the axis beyond the Courant's limit, leading to a drastic increase of memory required to store the field components. One way to reduce this burden is to exploit the angular periodicity of the structure and model only an individual slice, using appropriate conditions to simulate the effect of periodic replication. In the forty-mouse "ferris wheel" the unit slice is 9-degrees wide and contains only one animal. Because of the field uniqueness within the unit slice, it can be computed in the usual fashion except for the components that lay on the ϕ-boundaries. The latter can be updated by enforcing boundary conditions that equate field
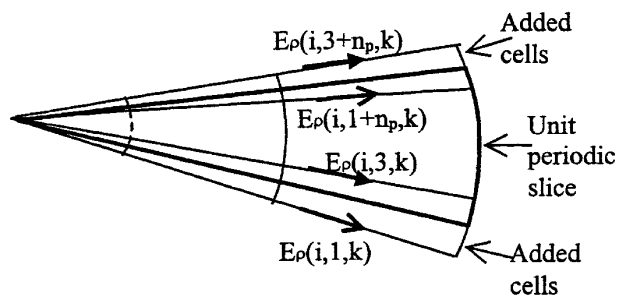

Fig. 5. Application of the periodicity condition to the ρ-component of the fields at the boundary of the FDTD grid. The unit-slice is n_p cells in the ϕ direction. For the application of the absorbing boundary condition, the FDTD grid needs to be two cells wider than n_p in the same direction.

components on one side ($\phi = \phi_0$) of the unit slice to those on the other side ($\phi = \phi_0 + \phi_p$), where ϕ_p is the periodic unit slice extension in the ϕ–dimension:

$$E_\rho\left(\rho,\phi_0,t\right) = E_\rho\left(\rho,\phi_0+\phi_p,t-t_d\right), \tag{6}$$

$$E_z\left(\rho,\phi_0,t\right) = E_z\left(\rho,\phi_0+\phi_p,t-t_d\right). \tag{7}$$

In general these periodic conditions depend on the field incidence angle on the structure [9]. Because the excitation is placed at the axis, there is no delay between ϕ-boundaries, thus $t_d = 0$ in (6)-(7). With a FDTD grid exactly equal to the unit slice it would not be possible to apply periodicity conditions because the fields in (6) and (7) would never be computed. For this reason, the FDTD grid we used is two cells wider than the unit slice, one more on each side, as shown in Fig. 5. The periodicity is enforced as follows

$$E_\rho\left(i,1,k\right) = E_\rho\left(i,1+n_p,k\right), \tag{8}$$

$$E_\rho\left(i,3+n_p,k\right) = E_\rho\left(i,3,k\right), \tag{9}$$

where i, k identify voxels in the ρ and z directions, respectively, while the components $E_\rho(i,1+n_p,k)$ and $E_\rho(i,2,k)$ are computed with the usual FDTD scheme. Analogous conditions are applied to the E_z, H_ρ and H_z components.

It should be observed that the above periodicity conditions become equivalent to a *perfect magnetic wall* (PMW) if, and only if, the unit slice is symmetric with respect of its bisecting centerline, e.g., when the dielectric load is centered about and symmetric around the centerline. In all other cases, including cavity loading by anatomical mice models, the PMW condition is not applicable.

Run -Time

The FDTD algorithm experiences numerical instability when the time-step is not chosen appropriately. To guarantee stability of the solution, the FDTD temporal step is related to the spatial step by the Courant stability criterion, which in cylindrical coordinates can be written [10]

$$\Delta t \leq \frac{1}{c}\left[\frac{1}{\left(\Delta\rho\right)^2}+\frac{1}{\left(\rho_{\min}\Delta\phi\right)^2}+\frac{1}{\left(\Delta z\right)^2}\right]^{-\frac{1}{2}}. \tag{10}$$

As a consequence, its upper bound depends on the very small cells surrounding the axis, so the computational time could become unacceptably high. However, if the E_ϕ component is not excited inside the structure, the temporal step does not depend on the minimum voxel dimension along ϕ and it can be made greater than the Courant limit without

inducing instability. In a "ferris wheel", the E_ϕ component can only be excited due to discontinuity introduced by the exposed animals and the cavity wall openings, which compromise the cylindrical symmetry of the structure. Near the $\rho = 0$ axis the E_ϕ component is indeed negligible because the animals are sufficiently far away. Therefore, the time-step can be made independent from the voxel dimension along ϕ of the innermost cells, which are also the smallest ones. We were able to choose a time-step twenty times greater then the Courant limit, with substantial run-time savings, without experiencing instability.

Modeling of the "ferris wheel"

As previously described, the "ferris wheel" exposure system is a 10-cm thick cavity loaded with forty mice The cavity radius is 48 *cm*, and the mice are placed 44 *cm* away from the center. Hence, only the 9-degree wide periodic slice, loaded by a dummy, is simulated. The FDTD model features a 79 x 27 x 75 (ρ, ϕ, z) spatial grid and 2 *ps* temporal step. The spatial step is variable in the ρ and z directions because most of the cavity is empty and therefore it can be discretized with a coarser spatial step than the region surrounding the dummies or the coax-to-cavity transition. In particular, the minimum step is approximately 3 mm for both frequencies that we have considered (900 MHz and 1.8 GHz). The dummy, centered on the bisecting line, is made of homogeneous tissue and has an ellipsoidal shape (7-cm major axis along z, 2.86-cm minor axis) very similar to the experimental dummies [5]. The space around the cavity is included in the model to determine RF leakage.

A uniaxial perfectly matched layer (UPML) terminated on a perfectly conductive plane [9] surrounds the FDTD space. The characteristics of the uniaxial medium are described by tensors. In the UPML medium the conductivity is coordinate dependent. In our code the conductivity has a polynomial scaling, e.g., in the ρ direction $\sigma_\rho(\rho) = (\rho/d)^m \sigma_{\rho\max}$, where d is the UPML thickness and m is arbitrary. We have chosen $m = 4$, and d equal to 6 FDTD cells. As pointed out in [11], the reflection coefficient of the PML in cylindrical coordinates cannot vanish identically for all radiated modes. However, for large $k_0\rho_0$ (k_0: free-space wavenumber, ρ_0: radial distance where PML layer starts) the reflection coefficient is negligible. The "ferris wheel" is an electrically large scatterer, so the PML reflection coefficient may be considered negligible.

In the FDTD model, ideal metallic surfaces with infinitesimal thickness are used for the cavity plates, the shorting posts and the circular caps of the coax-cavity transition. A different approach, featuring a modified form of the equation for the H$_\phi$ component, is used for the monopole and the counter poise to take into account their radii:

$$H_\phi^{n+1/2}\left(i+\tfrac{1}{2},j,k+\tfrac{1}{2}\right) = H_\phi^{n-1/2}\left(i+\tfrac{1}{2},j,k+\tfrac{1}{2}\right) -$$

$$\frac{\Delta t}{\mu_0 \Delta z}\left[E_\rho^n(i+\tfrac{1}{2},j,k+1)-E_\rho^n(i+\tfrac{1}{2},j,k)\right]+$$

$$\frac{\Delta t}{\mu_0 \Delta \rho}\frac{2}{\ln(\Delta\rho/a)}E_z^n(i+1,j,k+\tfrac{1}{2})\quad, \qquad (11)$$

where a is the monopole or counterpoise radius, while $\Delta\rho$ and Δz are Yee cell dimensions. As we can see from (11), the E_z component is not computed for cells surrounding the wires. For all other cells in the FDTD space near the axis, equation (3) was used.

We used a *one-way injector* to excite the structure. This kind of source [9] is simulated with a one dimensional 50 Ω transmission line as shown in Fig. 6, where an incident voltage is impressed at location k'$_{source}$. From this location a desired signal is launched in the forward direction (+z), while a negligible signal is launched in the backward direction (-z). At the cells where the coax-cable enters the cavity (i_a, j_a, k_a), the FDTD scheme is modified as follows:

$$H_\phi^{n+1/2}(i_a+\tfrac{1}{2},j_a,k_a+\tfrac{1}{2})=H_\phi^{n-1/2}(i_a+\tfrac{1}{2},j_a,k_a+\tfrac{1}{2})-$$

$$\frac{\Delta t}{\mu_0 \Delta z}\left[E_\rho^n(i_a+\tfrac{1}{2},j_a,k_a+1)-\frac{2}{\ln(\Delta\rho/a)}\frac{V_{k'_{top}}^n}{\Delta\rho}\right]+$$

$$\frac{\Delta t}{\mu_0 \Delta \rho}\frac{2}{\ln(\Delta\rho/a)}E_z^n(i_a+1,j_a,k_a+\tfrac{1}{2})\quad. \qquad (12)$$

4.   EXPERIMENTAL VALIDATION SET-UP

Return loss measurements of the "ferris wheel" loaded with forty dummy mice [5], reported in Fig. 7 for convenience, show that it is possible to achieve good impedance match to the 50-Ω source for a wide range frequencies and loading. In order to validate the FDTD code, further measurements
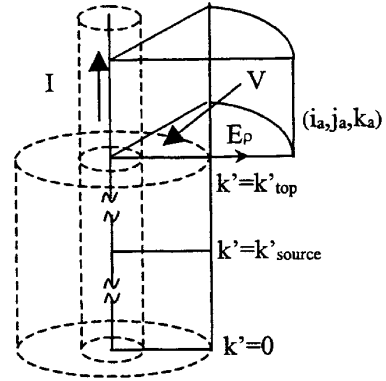

Fig. 6 One-dimensional transmission line for the one-way injection feeding system. One of the wedge cells where the voltage is injected is also shown.

were carried out by inserting a miniature field probe between the shorting posts and measuring the radial E-field distribution. The miniature probe features three small dipole sensors with rectifying diode detectors placed along three orthogonal directions in the so-called I-beam arrangement [12]. A TEM cell was employed to calibrate all three sensors separately. The probe was connected to an automated data acquisition system by IDX, Inc. Forward and reflected power were measured at the "ferris wheel" feed-point by means of a bi-directional coupler. The experimental set-up is sketched in Fig.8.

5.   RESULTS

The analysis is performed at 900 MHz, which is the original frequency for which the "ferris wheel" has been designed, as well as at 1.8 GHz to determine how much degradation is produced by higher-order mode excitation. Dielectric parameters of the dummies are $\varepsilon_r = 52$, $\sigma = 1$ S/m, and $\varepsilon_r = 50$,
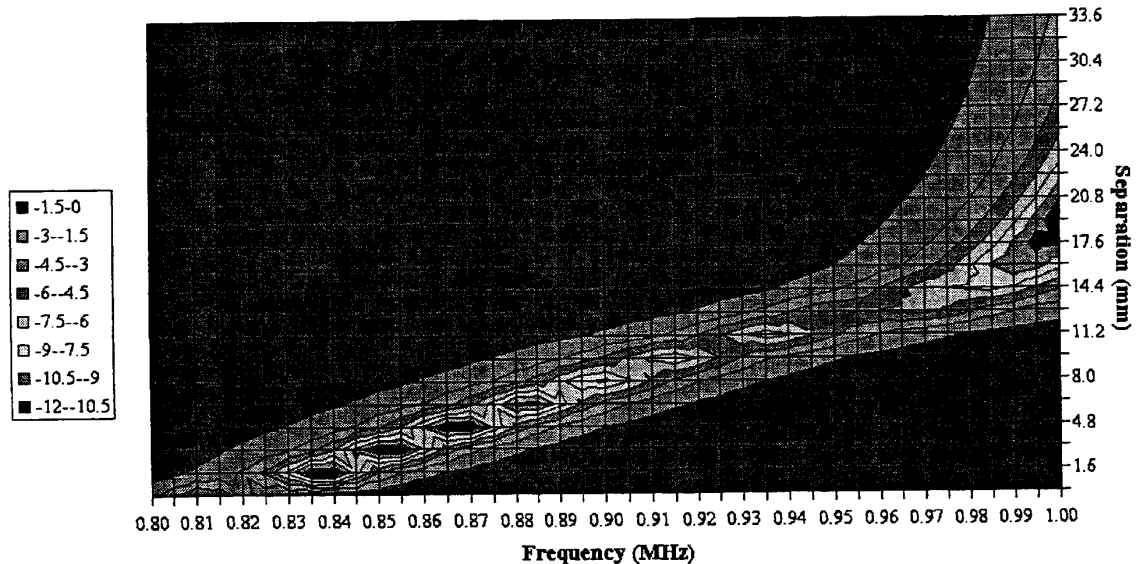

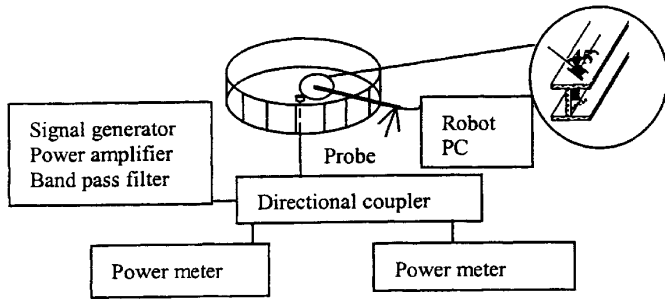*Fig.7 Measured return loss (dB) at the "ferris wheel" feed-point versus frequency and counterpoise separation.*

Fig.8 Measurement set-up for the radial distribution of the electric field at 900 MHz. The probe is inserted inside the cavity between two posts and is moved in a radial direction. The E-field probe (I-beam sensor arrangement) is sketched.

σ = 1.5 S/m, respectively. These are simulated muscle mixture parameters commonly used for FCC-mandated SAR compliance testing (http://www.fcc. gov/fcc-bin/dielec.sh). The spatial and temporal steps chosen are the same in both cases. At 1.8 GHz, the step inside the dummies (3 mm) is approximately $\lambda/8$, which is larger than the recommended step size ($\lambda/10$) for reducing numerical dispersion. Because of the mice small size, the dispersion involved with this step is acceptable. In the other regions the step is well below the dispersion limit.

As with any FDTD code, run-time is extremely machine dependent. The simulation time was three hours on a Digital Alpha 500 (400 MHz).

Numerical results at 900 MHz

Simulations were performed at 900 MHz for different positions of the tuning counterpoise, computing the cavity return loss with respect to the 50-ohm source. In Fig. 9, a comparison between measured and simulated return loss versus counterpoise position shows good agreement. The offset is just 1 *mm*, which is probably due to uncertainty of
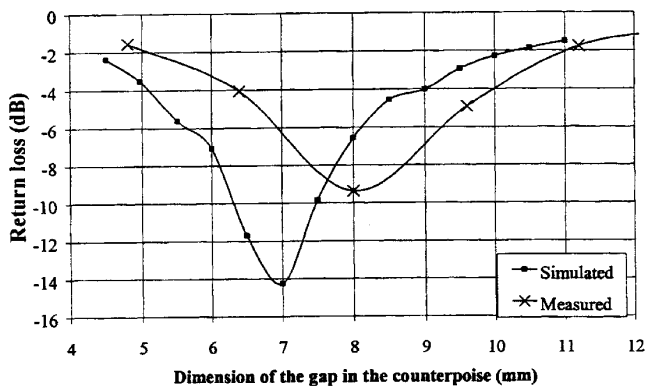

Fig.9 Comparison between measured and simulated return loss versus counterpoise distance at 900 MHz. The spatial discretization of the one-way injector transmission line is 4 mm, the same of the cell where it enters the coaxial cable.

distance measurement and neglecting of the two small caps thickness (Fig.3). The prediction accuracy of the return loss value is satisfactory, since the net input power difference amounts to less than 15% at the best match. Such a small discrepancy could be due to the ideal materials considered in the simulation and to uncertainties of the dummies dielectric parameter. Another source of uncertainty could be associated with the description of the region where the co-axial feed-line enters the cavity. Changing the simulated source (e.g., one-way injector to gap-source) changes the value of the calculated impedance as shown in Fig.10.
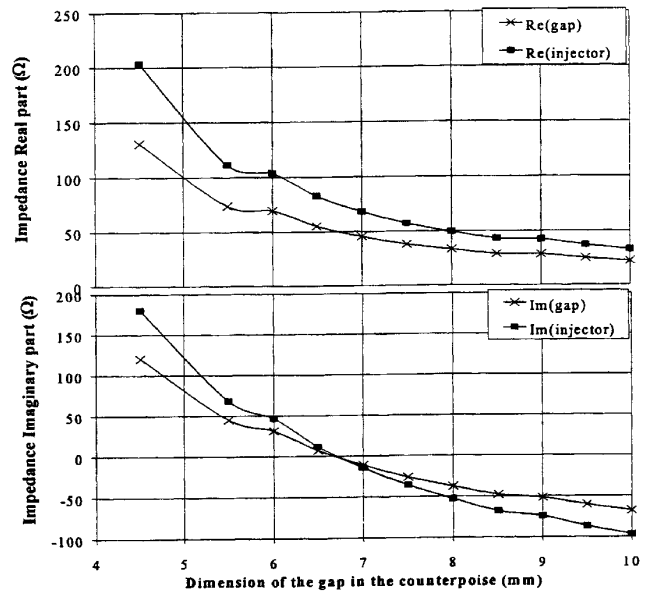

Fig.10 Input impedance of the "ferris wheel" for different source models: one-way injector, and gap-source model. The injector is modeled as in the previous figure. The gap is modeled with one 3.5-mm cell. In the latter case, the impedance is strongly affected by the gap-source dimension.

The spatial discretization of the excitation region also plays a critical role in determining the feed-point impedance. The results presented were derived using this spatial step: one 5 *mm*-radius cell for the smaller cap (d_1 in Fig.3), two 5 *mm*-radius cells for the other one (d_2 in Fig, 3), and variable cell size (2 *mm* to 3 *mm* along z) for the distance s. Moreover, for the one-way injector of Fig. 6, the spatial steps of the (i_a,j_a,k_a) cell are 5 *mm* along ρ, 4 *mm* along z. The angular step is uniform ($\Delta\phi = 0.375°$).

For best match conditions, a comparison between the measured and calculated radial distribution of the total field inside the cavity was performed. The results reported in Fig.11, which are normalized to the same net input power (0.3 W), show a very good agreement. Looking at the radial VSWR, they also indicate that the structure stores a good amount of reactive energy, as confirmed by its relatively narrow impedance bandwidth.
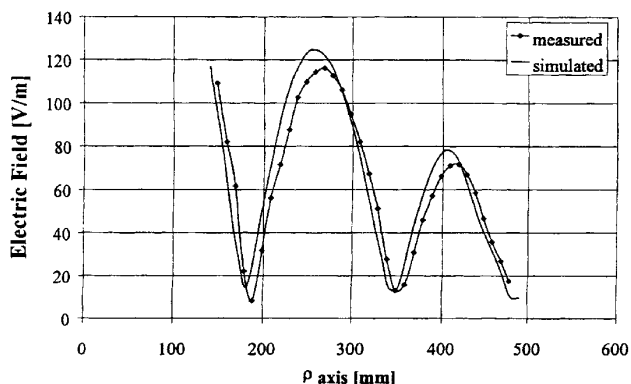
Fig.11 Comparison between simulated and measured total electric field radial distribution at 900 MHz. The radial line where results are compared runs between dummies. The data begin at 15 cm from the axis of the system, since the probe could not measure closer to the cavity center due to the presence of a hollow Teflon ring [5].

Analysis of exposure uniformity

In the initial design of the "ferris wheel" [5], uniformity of the SAR distribution inside the dummies was verified experimentally by means of thermographic measurements. However, thermographs allow quantitative analysis only across selected cut-planes. The FDTD code developed in this study provides a tool to carry out such an analysis on the entire volume of the exposed body, providing more insightful information regarding the SAR distribution. A quantitative criterion for uniformity is necessary for evaluating the exposure system performance. We chose to observe the deviation of local SAR, computed at every FDTD voxel in the dummy, from the whole body average SAR.
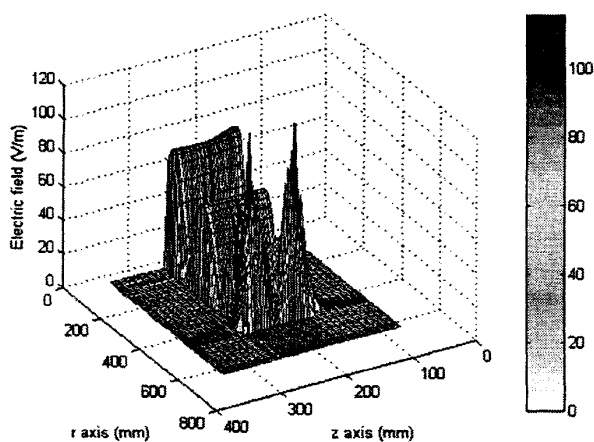
In Fig.12 the electric field inside the loaded cavity exhibits the typical pattern of a stationary wave inside a radial resonator. The field amplitude decreases as it penetrates the animal, but increases again at the other side of the animal because of Eddy currents and wave reflection at the posts shorting the cavity. The delivered power in this example is 50 mW. The power radiated through the circular holes and the lateral walls amounts to about 0.4 mW, which is less then 1% of the delivered power. This result is in excellent agreement with measurement [5] and demonstrates the ability of the "ferris wheel" to trap electromagnetic energy within the cavity at 900 MHz. Figure 13 shows the SAR inside the dummies on the central ρ-z cut-plane. The maximum peak SAR inside the dummy is 0.145 W/Kg. The whole body average SAR is 0.041 W/Kg.

The SAR distribution in the exposed body is quantified in Fig.14, where the percentile difference between the local and the whole body average SAR is plotted versus the number of voxels in the FDTD model of the dummy. For instance, we may want to determine how many voxels feature a SAR level lower than 40% of the whole-body average. As shown in the graph, we would find 448 voxels, corresponding to almost 35% of the animal tissue. Moreover, we notice that only 0.3% of the tissue has a SAR level of 200 % of the average. We should observe that a higher spread of the SAR distribution is to be expected in the case of real mice, since the markedly non-homogeneous dielectric properties due to the anatomical configuration of the mouse body parts would yield a wider SAR variations.

Results at 1.8GHz

Many wireless services operate in the frequency range between 1700 MHz and 1900 MHz, e.g., GSM in Europe. The exposure system was simulated at 1.8 GHz to analyze the uniformity of the SAR distribution at this frequency. The
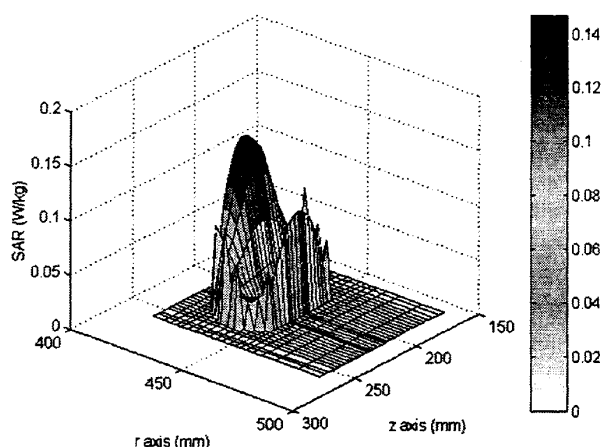

Fig.12 Distribution of the total electric field inside the loaded cavity for the ρ-z cut through the middle of the dummy (900 MHz). Two high-field spots occur at the cavity openings near the extremities of the dummy.

Fig.13 SAR distribution for the ρ-z cut through the middle of the dummy (900 MHz). Note that the distribution decreases with the ρ coordinate and then increases again due to the reflection at the shorting posts
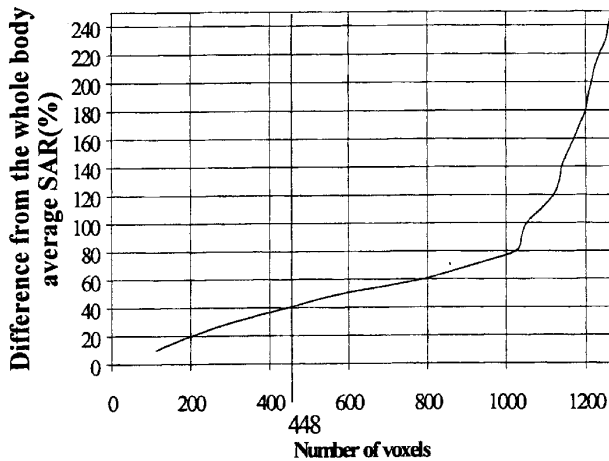
Fig.14 Percentile differences from the whole-body average SAR level vs. voxel number at 900 MHz. The curve can be seen as the cumulative distribution of the SAR function. The total number of cells is 1263. In the example, there are 448 voxels inside the dummy with a SAR level that is lower then 40 % of the whole body average SAR.

dimensions of the "ferris wheel" are such that modes exhibiting z-variation are above cut-off. Therefore a performance degradation in terms of field (and consequently SAR) uniformity is expected. Nevertheless, we addressed this analysis with the purpose of providing useful information for future reference in case the "ferris wheel" is used in animal studies at 1.8 GHz.

In Figs. 15 and 16 we show the distribution of the electric field and the SAR inside the cavity and the dummy, respectively. The plane considered is the same as in the previous case. As expected, we can see that the field is not uniform in the z direction. As a likely consequence of the
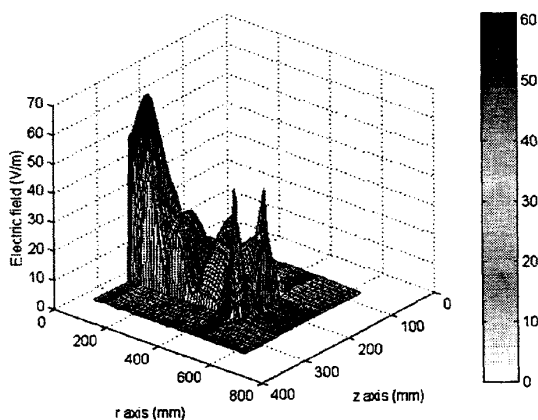
interference patterns of forward and reverse waves, the SAR distribution is remarkably concentrated inside the dummy. In this case, the RF power delivered to the cavity is 18 mW, and the power radiated through the hole and the posts is almost 3.6 mW, or about 2% of the delivered power. As expected, at higher frequency the power radiated outside is higher than before, due to the larger electrical size of the openings in the cavity walls.

The percentile difference in SAR level versus voxel number is plotted in Fig. 17. As a comparison with the previous case, consider the number of voxels exhibiting a SAR level lower than 40% of the whole body average. From the figure we can see that almost 42% of tissue falls in this condition, which seems to suggest that at 1.8 GHz the "ferris wheel" behaves better than at 900 MHz. However, we must consider that 3% of the tissue has a SAR level within a range of 300% to 500% of the whole body average. For this reason, redesign of the system for this frequency range may be needed. For instance, mode filters may reduce field variations due to longitudinal higher-order mode excitation, and mice positioning (distance from the boundary) could be optimized to attenuate SAR variations due to incident and reflected wave interference.

6.   FINAL REMARKS

The "ferris wheel" mice exposure system has been modeled in order to yield a numerical tool that allows efficient dosimetric analysis during the system's design. A FDTD code was developed in cylindrical coordinates, featuring solutions that dramatically decrease computation time and memory requirement. The code was validated with measurements on the real system with good results, which could improve using finer resolution to discretize the feeding system. The exposure system has been analyzed at 900 MHz, the original design frequency, as well as at 1.8 GHz
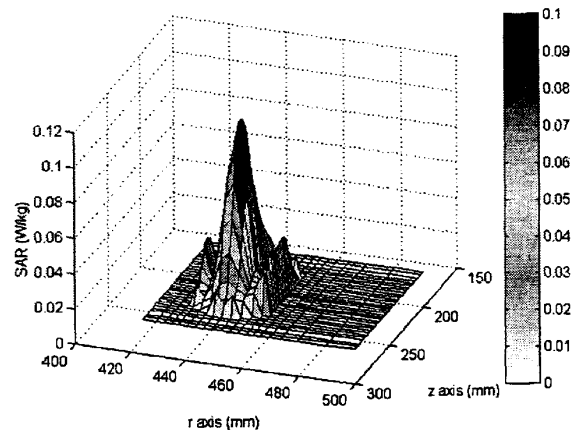

Fig.15 Distribution of the total electric field inside the cavity for the ρ-z cut through the middle of the dummies (1.8 GHz). Note that the field distribution is no longer TEM like, exhibiting variations in the z direction.

Fig.16 SAR distribution across the ρ-z cut passing through the middle of the dummy (1.8 GHz). The SAR is mainly concentrated at the center of the dummy, causing degradation of the SAR uniformity.
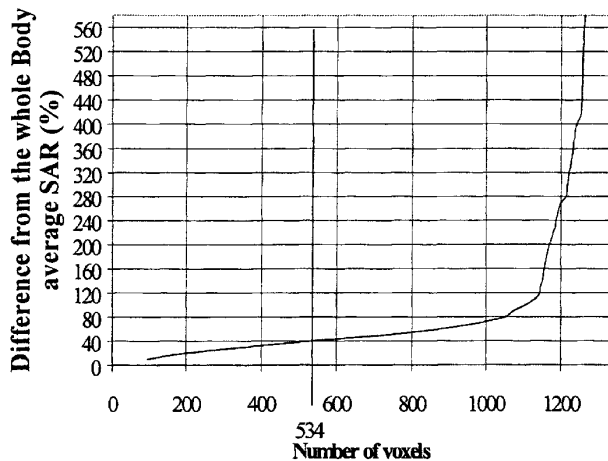
Fig.17 Differences (%) from the average SAR level vs. number of voxels at 1.8 GHz. At this frequency, 534 cells exhibit SAR lower than 40% of the whole body average.

for reference in future developments. We looked at the uniformity of the SAR distribution inside a dummy element for these two frequencies, and in particular characterized the SAR uniformity by quantifying the amount of tissue exhibiting a local SAR level that differs from the whole body average SAR. More uniform SAR distribution was observed at 900 MHz than at 1.8 GHz. It is interesting to notice that in both cases more than half of the tissue mass exhibits local SAR greater than the whole body average. In other words, the *median* SAR is greater than the *average* SAR. Such an observation cannot be generalized at this moment, since it is based on specific body geometry and composition, and under particular exposure conditions. In the future, the analysis will be repeated on anatomical models of mice to provide additional data on the uniformity of the SAR distribution. Nevertheless, at the design stage, use of homogeneous dummy mouse models has been found to be extremely efficient, as it allowed direct correlation with measurements, where dummy phantoms had to be used because of the practical impossibility of using a large number of live or dead mice.

ACKNOWLEDGMENTS

REFERENCES

[1] J. A. D'Andrea, J. R. DeWitt, O. P. Gandhi, S. Stensaas, J. L. Lords, H. C. Nielson, "Behavioral and physiological effects of chronic 2,450-MHz microwave irradiation of the rat at 0.5 mW/cm2," *Bioelectromagnetics*, vol. 7, no. 1, pp. 45-56, 1986.
[2] C. K. Chou, A. W. Guy, L. L. Kunz, R. B. Johnson, J. Crowley, and J. H. Krupp, "Long-term, low-level, microwave irradiation of rats," *Bioelectromagnetics*, vol. 13, no. 6, pp. 469-496, 1992.
[3] M. H. Repacholi, A. Basten, V. Gebski, D. Noonan, J. Finnie, and A. W. Harris, "Lymphomas in Em-Pim1 transgenic mice exposed to pulsed 900 MHz electromagnetic fields," *Radiation Research*, vol. 147, pp. 631-640, 1997.
[4] C. K. Chou, H. Bassen, J. Osepchuk, Q. Balzano, R. Petersen, M. Meltz, R. Cleveland, J. C. Lin, and L. Heynick, "Radio Frequency Electromagnetic Exposure: Tutorial Review on Experimental Dosimetry," *Bioelectromagnetics*, vol. 17, pp. 195-208, 1996.
[5] Q. Balzano, C. K. Chou, R. Cicchetti, and A. Faraone, "An Efficient RF Exposure System with Precise SAR Estimation for In-Vivo Animal Studies at 900 MHz," *IEEE Trans. on Microwave Theory Tech.*, vol. 48, No. 11, pp. 2040-2049, Nov. 2000.
[6] A. Taflove, "Computational Electrodynamics: The Finite Difference Time Domain Method," *Artech House*, 1995.
[7] M. A. Fusco, M. V. Smith, L. W. Gordon, "A Three-Dimensional FDTD Algorithm in Curvilinear Coordinates," *IEEE. Trans. on Antennas Propagat.*, vol. 39, no.10, pp. 1463-1471, Oct. 1991.
[8] Y. Chen, R. Mittra, P. Harms, "Finite-Difference Time-Domain Algorithm for Solving Maxwell's Equations in Rotationally Symmetric Geometries," *IEEE Trans. on Microwave Theory Tech.*, vol. 44, no. 6, pp. 832-839, June 1996.
[9] A. Taflove, "Advances in Computational Electrodynamics: The Finite Difference Time Domain Method," *Artech House*, 1998.
[10] Q. Chen, V. F. Fusco, "Three dimensional Cylindrical coordinate Finite-Difference Time-Domain Analysis of curved slotline," *2nd Intl. Conference on Computation in Electromagnetics*, pp. 323 - 326, 1994.
[11] M. Kuzuoglu, R. Mittra, "Investigation of Nonplanar Perfectly Matched Absorbers for Finite-Element Mesh Truncation," *IEEE Trans. on Antennas Propagat.*, vol.45, no.3, pp. 474-486, March 1997.
[12] H. Bassen, M. Swicord, and J. Abita, "A Miniature Broad-Band Electric Field Probe," *Annals New York Academy of Sciences*, vol. 247, pp.481-493, 1975.